Heritage Science

RESEARCH

Open Access

Bloomery iron production in the Holy Cross Mountains (Poland) area during the Roman period: conditions during the metallurgical process and their uniformity between locations

Krzysztof Kupczak[1*], Rafał Warchulski[1], Aleksandra Gawęda[1] and Jan Janiec[1]

Abstract

The study assessed the uniformity of the metallurgical process carried out during the period of Roman influence in Poland. The age of the investigated material was confirmed based on an analysis of the $^{12}C/^{14}C$ isotope ratio in the charcoal found in slag. The comparison was based on four Holy Cross Mountains (Poland) locations. The evaluation included smelting temperature, viscosity of the metallurgical melt, oxidation–reduction conditions, and slag cooling rate determined based on geochemical (XRF) and mineralogical (XRD, SEM, EPMA) analyses. Despite the distance between individual sampling sites, the conditions in which smelting was carried out were similar for all samples. The liquidus temperature of the analyzed slags was in the range of 1150–1200 °C. Oxidation–reduction conditions were determined through thermodynamic calculations using SLAG software. In the temperature range of 1150–1200 °C, the oxygen fugacity had to be below $\log P_{O_2} = -13.20$ to -12.53 atm to reduce iron oxides to metallic iron. The viscosity of the metallurgical melt was calculated and ranged from 0.15 to 1.02 Pa s, indicating a low viscosity. The slag cooling rate determined based on olivine morphology was in the range of > 5 to 300 °C/h. Smelting parameters were compared with other locations in Poland, and similar results were obtained for slags from Masovia and Tarchlice. In the case of one site (Opole), despite the higher maximum value of liquidus temperature, it was indicated that the process could have taken place in similar conditions, and the differences resulted from contamination of the slag with material from the furnace/pit walls.

Keywords Slags, Iron, Process reconstruction, Smelting, Viscosity, Temperature, Oxygen fugacity

Introduction

Slags are waste materials generated during the smelting of metals using pyrometallurgical methods [1]. As a result of high temperature at a suitably reducing environment in the smelting furnace, a metallic phase (or intermediates) and a waste material (slag) can be formed [2].

In the case of many historical metallurgical centers, documentation describing the technical aspects of the metallurgical process is not available (e.g., [3–5]). Modern analytical methods based on determinations of the chemical and phase composition of metallurgical by-products, together with the use of experimental methods, allow to fill this gap by reconstructing the conditions under which the slags were formed and, thus, the conditions under which the smelting was carried out [6–13]. Since historical metallurgical processes often vary from location to location, there is no single path to follow during such archaeometric research. Thus, each studied material requires an individual approach.

*Correspondence:
Krzysztof Kupczak
krzysztof.kupczak@us.edu.pl
[1] Faculty of Natural Sciences, Institute of Earth Sciences, University of Silesia in Katowice, Będzińska 60, 41-200 Sosnowiec, Poland

Iron, however abundant, is rarely observed in a native state on the Earth's surface. Native iron has so far only been found in a few places, e.g., the volcanic rocks of Disko Island (Greenland), Siberian traps (Russia), and Miocene volcanic rocks in Central Germany (Bühl) [14]. Iron in metallic form can also be observed in iron meteorites, which consist mainly of Fe–Ni alloys [15]. Apart from these exceptions, Fe is overwhelmingly found on the Earth's surface as FeO and Fe_2O_3 to form many minerals [16].

The oldest objects made of iron date back to the 6th to 4th millennium BC and have been found in the Middle East and Egypt. Still, no reduction processes were carried out to form iron objects during this period, but meteorite iron was used for this purpose [17]. The first attempts to smelt iron from ores most likely come from the Anatolian area and are dated to the 2nd millennium BC. From the 16th to the twelfth century BC, the Hittite Empire was the only region where iron production was carried out. Over time, the ability of smelting Fe spread worldwide, reaching present-day Poland in about the second century BC [18]. The oldest Fe mining centers in Poland are related to the period of Roman influence and include, among others, the Holy Cross Mountains, Mazovia, Silesia, and Wołów regions [19]. The period of Roman influence refers to the age covering the 3rd period of the Iron Age in the area of the so-called Barbaricum (including the area of today's Poland). Even though the Roman Empire did not rule over the Barbaricum, its influence was significant and contributed to the development of local communities mainly through trade and knowledge exchange [20].

The Holy Cross Mountains region is the largest and best-known among Polish centers of ancient metallurgy thanks to the long-term research of Mieczyslaw Radwan, Kazimierz Bielenin, Szymon Orzechowski and others (e.g., [21, 22]). During archaeological works, tap slags, iron products, remains of furnace walls, places of ore storage, charcoal production, and items indirectly related to metallurgical production, such as ceramics, ornaments, and coins, were found [19, 21, 23]. Based on archaeological findings, it was possible to date them from 100 BC to 350 AD (mainly based on found ceramics and coins). The antique nature of the finds was confirmed by isotopic analyses, which yielded results in the range of 300 BC–400 AD [21]. Investigations in the area have revealed numerous remnants of former iron production in the form of smelter slags [21]. The region with the largest number of furnaces occupies an area of about 800 to 1000 km^2 [19]. About 8000 sites were discovered, with more than 550,000 furnaces. Slag fragments found in this area weighed up to 120 kg. Based on the amount of slags/pits found, it is estimated that about 11,000 tons of iron were produced in this area during the period of Roman influence [19]. The presence of numerous remains has contributed to the development of research into ancient iron production methods. They focused mainly on the impact of bloomery iron production on society and experimentally reproducing the process (e.g., [19, 21, 23]). Reconstructions have been focused on providing information on the composition of the smelter charge (proportions of ores and charcoal), the amount of charcoal used for smelting, and the efficiency of the process [21]. Still, only during experiments conducted since 2012 has it been possible to obtain materials equivalent to those produced in historical times [24]. Parameters such as melt viscosity or oxygen fugacity have not been analyzed so far [19, 21, 25].

The main goal of the presented work is to determine the uniformity of bloomery iron production based on the analysis of the conditions prevailing during smelting in selected locations. Geochemical, petrographic, and mineralogical methods allowed for the determination of the liquidus temperature of the slags, the viscosity of the silicate melt from which the slags crystallized, the oxidation–reduction conditions prevailing during the smelting, and the cooling rate of the slags. The obtained data made it possible to determine to what extent the conditions differed during bloomery iron production in the Holy Cross Mountains and to indicate the similarities in process conditions between the Holy Cross Mountains and other locations in Poland.

Samples were collected in the vicinity of the Skarżysko-Kamienna, Starachowice, and Iłża (Fig. 1; [26]). These cities are located in the northern part of the area where iron smelting was carried out during the Roman influence period [21]. Slags from this area have not yet been thoroughly analyzed. Sampling from several locations from an area exceeding 20 km in radius was crucial to ensure that the studied slags originate from different local metallurgical centers (Fig. 1).

In the area where the slags were found, oxide and carbonate iron minerals forming concretions are abundant [22, 27]. The best described are the youngest traces of iron ore mining covering the period of the eighteenth-twentieth centuries [28]. Knowledge about the older ones is based only on written historical sources, without the possibility of locating the mining sites [28]. Only one ancient mining site, i.e., the Rudki mine, has been recognized (Fig. 1). Modern (since 1922) mining has revealed traces of ancient exploitation in the upper, weathered part of the Rudki deposit. Archaeological investigations led to the discovery of tools (shovels, spoons, shells of broken pots) in old mining pits [21]. Most probably, a range of smaller deposits were also exploited in this area [21, 23], especially in locations farther from the Rudki

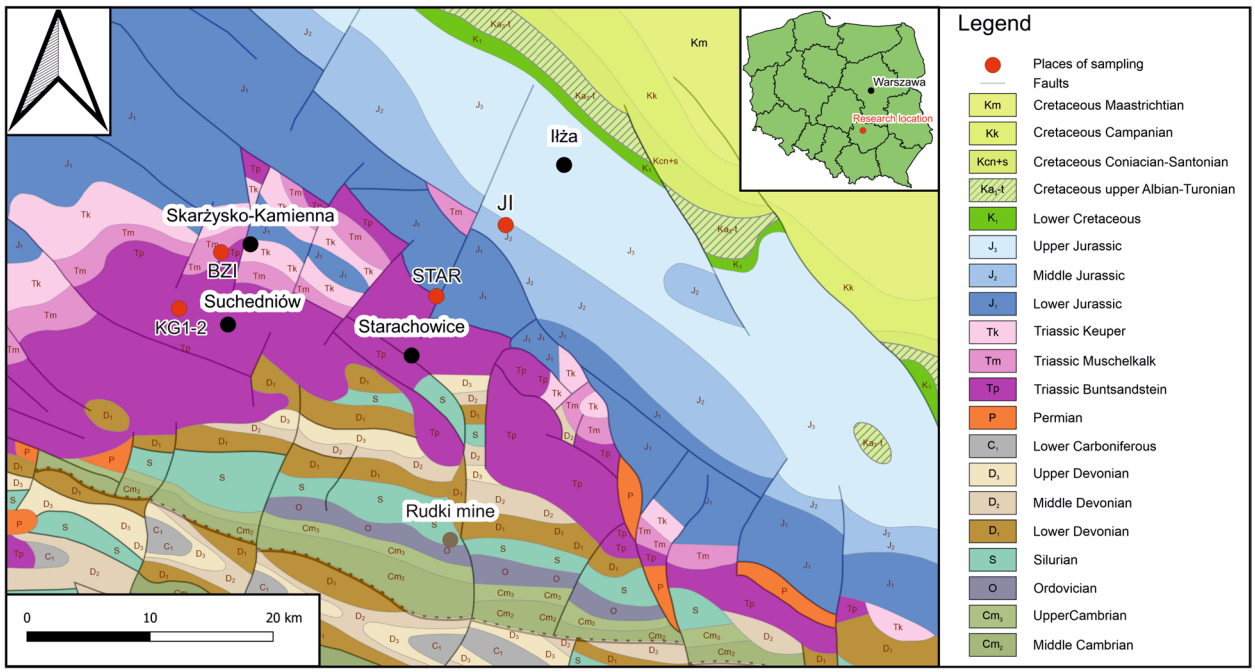

Fig. 1 Geological map showing sampling sites. Prepared based on data available on geoportal.gov.pl [31]

mine [21]. Near Starachowice and Suchedniów, hematite ores occur in Triassic deposits. Triassic and Middle Jurassic clay siderites also occur near Starachowice [21]. Limonite deposits and bog iron also occur in the analyzed area [22].

Materials and methods

Sampling

During the research, slags were collected from the area around the cities located in the Świętokrzyskie Voivodship: Suchedniów (KG1-2), Skarżysko-Kamienna (BZI), Iłża (JI) and one slag sample was obtained from the Museum of Nature and Technology in Starachowice (divided later into two subsamples; STAR1-2; Figs. 1, 2). Samples KG1 and KG2 were collected from two different pits located in close proximity (several dozen meters). The analysis of two samples found close to each other made it possible to check whether there were differences in metallurgical conditions between smelts conducted within one location. Prior to advanced petrological and geochemical analyses, representative samples were chosen from each location based on macro- and microscopic observations (optical microscope and SEM). Nonweathered material from the central part of the slag pieces with typical macro- and microscopical images was selected for further analysis. The samples were crushed, ground, and quartered to obtain the proper amount for chemical and phase composition analyses. Additionally, thin sections were prepared for microscopic observations. After preliminary data was obtained for the STAR sample, it was decided to separately analyze two subsamples (STAR1 and STAR2) differing in terms of chemistry and phase composition.

Chemical and phase analyses

The first step of the analysis was the macroscopic and microscopic observations to assess the slag's texture. An Olympus BX-51 polarizing microscope and a scanning electron microscope (The Phenom XL) equipped with an energy dispersive spectrometer (SEM–EDS) were used for this purpose (Institute of Earth Sciences, University of Silesia). An electron micro-probe (Cameca SX100, Inter-Institutional Laboratory of Microanalysis of Minerals and Synthetic Materials, University of Warsaw) was used to determine the exact chemical composition of the phases. Electron micro-probe analyses were performed at 15 keV accelerating voltage, a 10–20.1 nA beam current, and a beam diameter of up to 5 µm. Approximately 130 analyses of the chemical composition of phases occurring in the analyzed slags were performed, most of which (approx. 90) were performed for olivine crystals. The FeO to Fe_2O_3 ratio in spinel crystals was calculated to balance unit cells ($A^{2+}D^{3+}{}_2O_4$); similar calculations were performed for iscorite crystals. Details on detection limits and measurement parameters are available in Additional files 1, 2.

The phase composition of the samples was determined using the PANalytical X'PERT PRO-PW 3040/60 X-ray

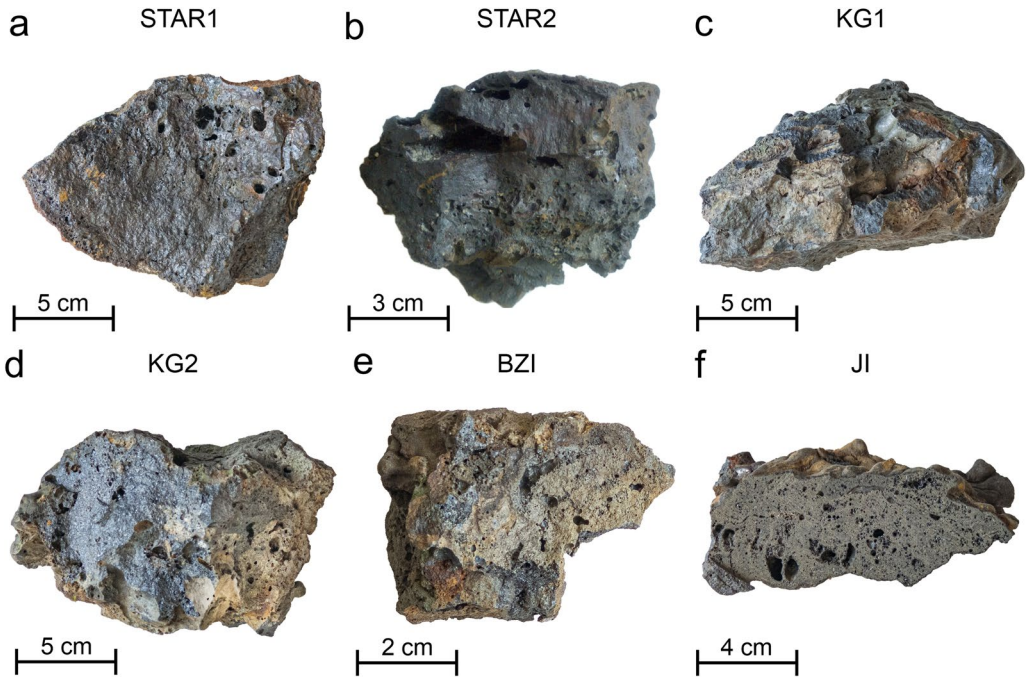

Fig. 2 Macroscopic photos of the analyzed slags

diffractometers (XRD) equipped with $CoK_{\alpha 1}$ source radiation and Fe-filter to reduce the K_{β} radiation. During analyses, the X'celerator detector was used (Faculty of Natural Sciences, University of Silesia). The analyses were performed in the 5–90°2Θ angular range at 40kv voltage (40 mA). For quantitative phase composition, a Rietveld analysis was performed using the X'PERT High Score Plus software with the PDF4 + database [29].

The slags' chemical composition was determined using X-ray fluorescence (XRF) by Bureau Veritas Mineral Laboratories (Canada) on fused discs according to XF702 program. For trace elements, the samples were digested with Aqua Regia and analyzed using ICP ES/MS method by Bureau Veritas Mineral Laboratories. Quality assurance/quality control was calculated based on duplicates and reference materials analyses. Details about quality assurance/quality control (QA/QC) are presented in Additional file 3.

Dating

A radiocarbon dating method was used to estimate the age of the analyzed material. For this purpose, about 1.5 g of charcoal was taken from the STAR1 sample. The charcoal was then processed into graphite and analyzed for $^{14}C/^{12}C$ isotope ratio using an Accelerator Mass Spectrometer (AMS). The CEMIZ Isotope Methods Center in Gliwice carried out AMS analyses. The radiocarbon dates were calibrated using OxCal 4.4 software [30] using the IntCal20 calibration curve [31]. Only the STAR1 sample was used for dating because it was the only one in which charcoal fragments were found.

Software

Graphical spatial (QGIS), raster (Adobe suite), and vector (Corel suite) data processing software were used during this research. SLAG software [32] was also used to determine the thermodynamic equilibrium between metallic Fe and FeO. QGIS and SLAG software were available with an open-source license. Adobe and Corel DRAW software were used with an educational license.

Results

Slag characteristics

Bulk chemistry

Slags reveal consist mainly of FeO (43.97–75.32 wt.%) and SiO_2 (18.04–47.14 wt.%), while minor components are Al_2O_3 (3.67–4.83 wt.%), CaO (0.50–2.47 wt.%), MnO (0.39–3.91 wt.%), P_2O_5 (0.04–1.76 wt.%), and K_2O (0.46–1.39 wt.%; Table 1). Small (less than 1 wt.% of oxide) amounts of TiO_2, MgO, and Na_2O were also detected (Table 1). The negative LOI (Loss on Ignition) values result from iron oxidation at 1000 °C (Table 1). Since the slags are composed mainly of FeO, the LOI values exceeded the limits in most cases (± 5.1 wt.%; Table 1). The concentrations of trace elements (e.g., V, Cr, As, Zn,

Table 1 Chemical composition of slags

		STAR1	STAR2	KG1	KG2	BZI	JI
SiO_2	wt.%	18.04	47.14	28.24	18.53	26.00	22.56
TiO_2		0.16	0.22	0.21	0.17	0.18	0.14
Al_2O_3		3.67	3.83	4.83	4.08	4.33	3.68
FeO		75.32	43.97	56.56	68.25	60.51	68.05
MnO		0.52	0.39	3.38	2.96	3.91	2.16
MgO		0.41	0.32	0.75	0.66	0.64	0.35
CaO		0.50	0.77	2.47	1.86	1.44	0.74
Na_2O		0.05	0.17	0.05	0.03	0.04	0.03
K_2O		0.46	0.94	1.39	0.92	1.00	0.57
P_2O_5		0.04	0.10	1.75	1.54	1.76	0.57
TOT/C		0.03	0.04	0.03	0.03	0.09	0.05
TOT/S		0.05	0.08	< 0.02	< 0.02	< 0.02	< 0.02
Total		99.25	97.97	99.66	99.03	99.9	98.9
LOI		< – 5.1	– 3.4	< – 5.1	< – 5.1	< – 5.1	< – 5.1

LOI: loss on ingnition; TOT/C: total carbon; TOT/S: total sulphur

Pb) in the analyzed slags did not exceed 130 mg kg^{-1} (Additional file 3).

Macro- and microscopic image and phase composition

Macroscopically, the collected slags have a steel-gray color. The surface of all slags shows traces of weathering in the form of a lighter in color or grayish-orange layer reaching a maximum of 1–2 mm deep into the samples (Fig. 2). Numerous pores were observed within slags, rarely exceeding 10–30 mm in diameter (Fig. 2). STAR1 sample was also characterized by the presence of unburned charcoal in the slag. Flow traces were observed on the surface of all samples, but they are best visible in the JI sample (Fig. 2f). Macroscopically, the slags appear entirely crystalline. However, microscopic observations showed the presence of amorphous phases in the samples.

The STAR1 sample consists of olivines ($(Fe, Mg)_2SiO_4$; 60.5 vol.%), wüstite (FeO; 27.0 vol.%), spinels (8.2 vol.%), and leucite ($KAlSi_2O_6$; 4.3 vol.%; Figs. 3; 4). Hypocrystalline and crystalline zones were distinguished in the sample. In zones with a hypocrystalline texture, olivines ($(Fe, Mg)_2SiO_4$) are dispersed within the glass as subhedral, mainly tabular or elongated crystals (Fig. 4b). In contrast, within fully crystalline zones, olivine is the main phase, while oxide phases and leucite are scattered between them (Fig. 4a). Spinel was observed mainly as subhedral crystals, reaching about 100 µm in size (Fig. 4a). Wüstite occurs mainly as small (up to 30 µm) oval grains (Fig. 4a), and leucite as anhedral crystals up to a few tens of µm in size (Fig. 4a).

The STAR2 sample consists of a high content of quartz (46.0 vol.%), cristobalite (1.8 vol.%), and lower (25.8 vol.%) content of fayalite compared to other samples (Fig. 3). This sample also contained leucite (2.1 vol.%), feldspar, and zircon ($Zr(SiO_4)$; Figs. 3, 4c, d). In the STAR2 sample, three distinct zones were observed (Fig. 4c). The first one contained mainly olivine, which filled the vast majority of the sample (Fig. 4c). Spinel, leucite, and wüstite crystals were also observed in this zone. The second zone in the STAR2 sample is the zone composed mainly of SiO_2 phases and glass (Fig. 4c). In this zone, feldspars with a diameter of up to 200 µm and zircon crystals measuring up to 30 µm in length and 10 µm in width also occur sporadically (Fig. 4c, d). Between the zone composed mainly of olivine and the one composed mainly of quartz, there is an area containing olivine crystals dispersed in the glassy phase, up to about 200 µm long and several µm wide (Fig. 4c). Since the STAR2 sample contains both quartz and leucite (Fig. 3), which cannot co-crystallize from the melt, it was concluded that the sample is contaminated by the fragments of the furnace/pit walls. For this reason, it was excluded from further investigations aiming to recreate conditions during the smelting process.

In KG1, olivines account for 74.7 vol.% of the sample (Fig. 3). They were observed as tabular crystals up to 200 µm in length, dispersed in the glass (Fig. 4e). Leucite (6.0 vol.%; Fig. 3) was observed in the form of crystals up to 100 µm in size (Fig. 4e). Sporadically, in KG1 slag iscorite ($Fe^{2+}{}_5Fe^{3+}{}_2SiO_{10}$) occurs in the form of elongated crystals (up to several hundred µm in length; Fig. 4g). The oxide phases in sample KG1 are represented by wüstite (oval crystals up to 30 µm in diameter; 10.5 vol.%; Figs. 3; 4f) and spinel (crystals up to 100 µm in size; 8.2 vol.%; Figs. 3; 4f).

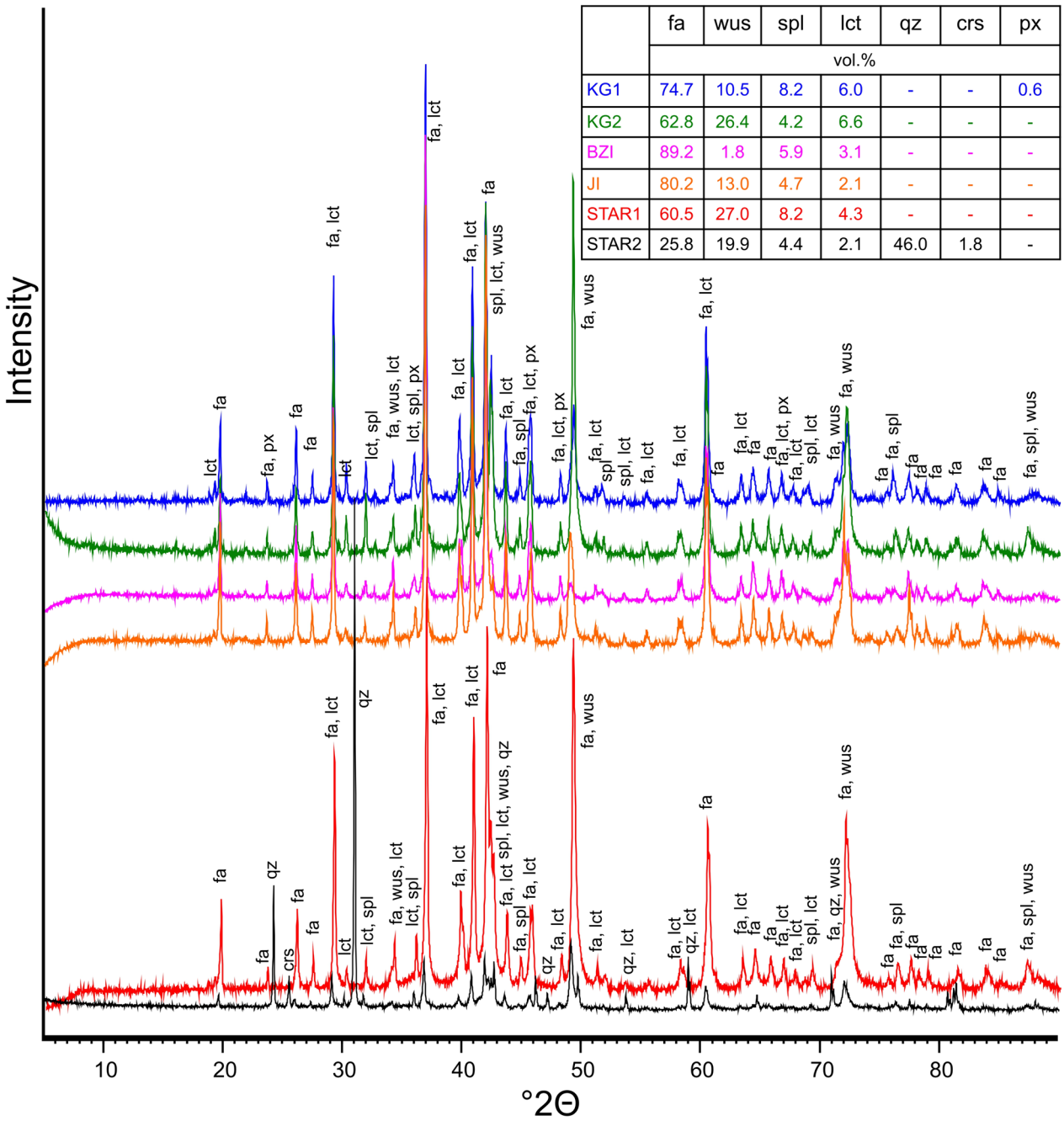

	fa	wus	spl	lct	qz	crs	px
	vol.%						
KG1	74.7	10.5	8.2	6.0	-	-	0.6
KG2	62.8	26.4	4.2	6.6	-	-	-
BZI	89.2	1.8	5.9	3.1	-	-	-
JI	80.2	13.0	4.7	2.1	-	-	-
STAR1	60.5	27.0	8.2	4.3	-	-	-
STAR2	25.8	19.9	4.4	2.1	46.0	1.8	-

Fig. 3 Results of XRD analysis of slags. crs: cristobalite; fa: fayalite; lct: leucite; px: pyroxene; qz: quartz; spl: spinel; wus: wüstite

In sample KG2, olivine (62.8 vol.%; Fig. 3) is present as the main phase, with wüstite (26.4 vol.%; Fig. 3) and spinel (4.2 vol.%; Fig. 3) crystals scattered within the sample (Fig. 4h). Wüstite occurs as oval grains up to 20 µm in diameter (Fig. 4h). Spinel occurs as crystals up to 80 µm in size (Fig. 4h). Sporadically leucite crystals (6.6 vol.%) were also observed (Fig. 3).

In the BZI sample, olivine (89.2 vol.%; Fig. 3) was most commonly observed as elongated, 30–50 µm wide crystals with glass or small (up to a few µm in diameter) spinel crystals between them (5.9 vol.% of the sample; Figs. 3; 4i). Less frequently olivine formed tabular crystals reaching several hundred µm in size (Fig. 4j). Oval wüstite crystals were also observed (1.8 vol.%; Fig. 3) throughout

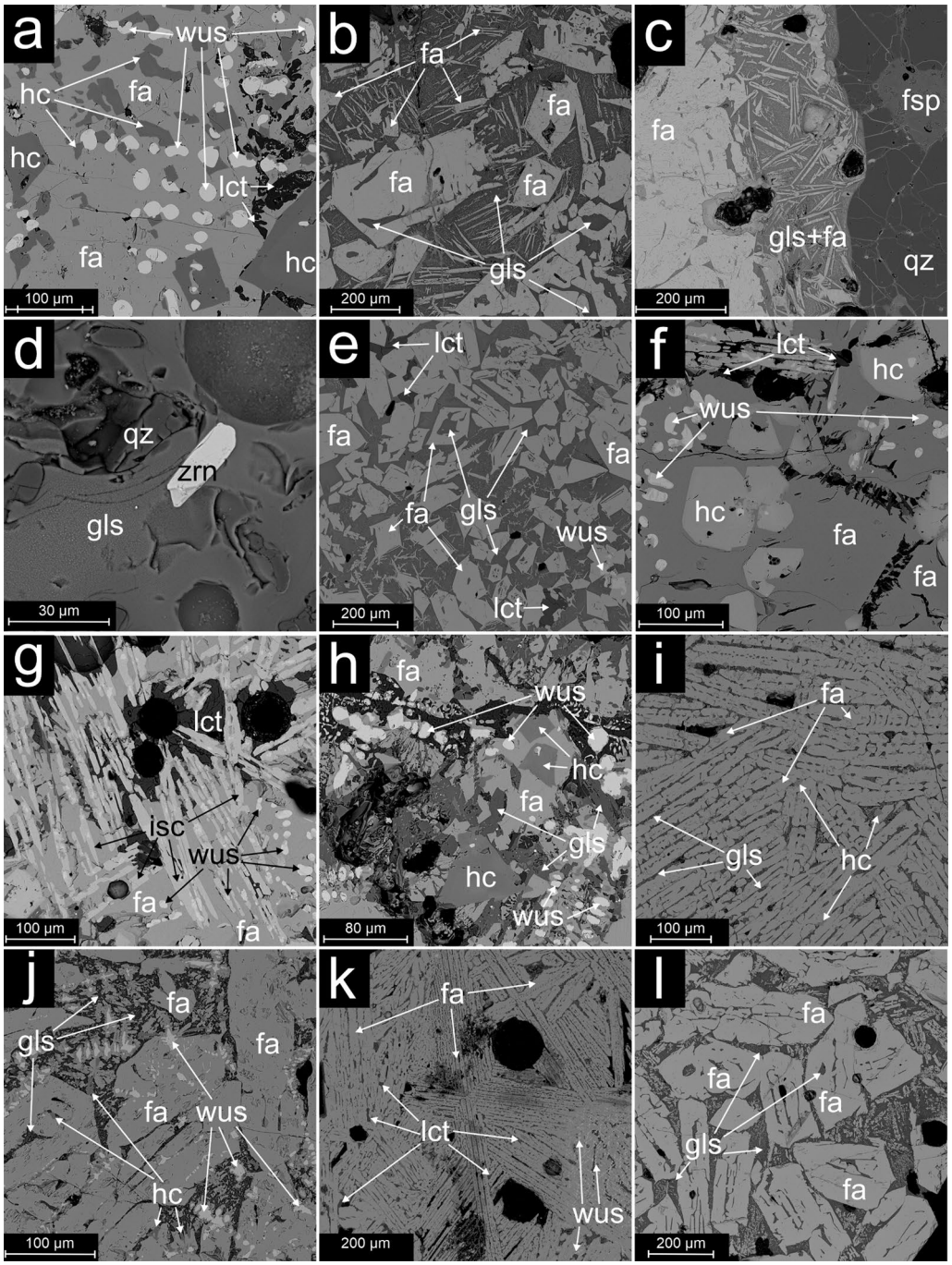

Fig. 4 BSE (back-scattered electrons) images of the slag samples: **a**, **b**—STAR1, **c**, **d**—STAR2 **e**–**g**—KG1; **h**—KG2; **i**, **j**—BZI; **k**, **l**—JI. fa: fayalite; fsp: feldspar; gls: glass; hc: hercynite (spinel); isc: iscorite; lct: leucite; wus: wüstite; zrn: zircon

the sample, with diameters mostly not exceeding 20 µm (Fig. 4j).

In the JI slags, elongated olivine (80.2 vol.%; Fig. 3) reaching several hundred µm in length was observed (Fig. 4k). Less frequently, olivines were observed as tabular crystals up to 200 µm (Fig. 4l). The presence of wüstite (13.0 vol.%) in the form of small (less than 10 µm) oval phases, spinel (4.7 vol.%), and leucite (2.1 vol.%) was found within the sample (Fig. 3).

Phase chemistry

Silicates and aluminosilicates The main silicate phase is olivine with a chemical composition corresponding to fayalite (Fe_2SiO_4; 57.7–67.6 wt.% of FeO; Table 2). Within fayalite, substitutions of Mn (0.76–7.4 wt.% of MnO), Al (0.16–0.31 wt.% of Al_2O_3), and Ca (0.18–1.67 wt.% of CaO) were commonly observed (Table 2). Iscorite crystals were also observed in the analyzed slags. In iscorite substitution of Al (up to 2.8 wt.% of Al_2O_3) and Mn (up to 1.45 wt.% of MnO) was found (Table 2). The only aluminosilicate phase observed in the slags was leucite, with the substitutions of Fe (up to 0.96 wt.% of FeO), Ba (up to 0.22 wt.% of BaO), Na (up to 0.10 wt.% of Na_2O; Table 2).

Oxides Oxide phases in the analyzed slags were observed as wüstite, spinel, and quartz. Spinel occurs as phases with a chemical composition corresponding to the magnetite ($Fe^{2+}Fe^{3+}{}_2O_4$)-hercynite ($Fe^{2+}Al_2O_4$) solid solution with the additions of Ti (0.49–1.08 wt.% of TiO_2), and Mn (0.56–1.28 wt.% of MnO) (Table 2).

Table 2 Representative chemical composition of phases occurring in slags

	ol1 BZI	ol2 JI	ol3 KG1	ol4 KG2	ol5 STAR1	qz KG1	leuc KG1	isc KG1	spl1 KG2	spl2 JI	spl3 BZI	gls (n = 16) KG1	gls (n = 23) BZI
SiO_2	29.6	29.1	30.4	29.4	29.7	98.6	56.4	9.1	0.39	0.78	0.45	44.93 ± 3.79	40.70 ± 2.95
TiO_2	bdl	bdl	bdl	0.07	bdl	bdl	bdl	0.29	0.85	1.08	0.49	0.60 ± 0.14	0.90 ± 0.12
Al_2O_3	0.19	0.25	0.17	0.31	0.16	bdl	23.2	2.8	47.5	10.3	0.4	15.81 ± 1.84	20.65 ± 2.41
Fe_2O_3* -	–	–	–	–	–	–	–	25.9	13.3	54.6	68.7	20.05 ± 3.07	18.94 ± 1.86
FeO	63.2	66.4	59.8	57.7	67.6	bdl	0.96	59.9	35.8	31.4	31.15	–	–
MnO	4.8	2.7	6.6	7.4	0.76	bdl	bdl	1.45	1.28	1.03	0.56	1.40 ± 0.15	0.97 ± 0.25
MgO	1.39	0.79	2.6	1.68	1.26	bdl	bdl	0.4	0.1	0.2	bdl	0.08 ± 0.06	0.09 ± 0.02
CaO	0.18	0.20	0.57	1.67	0.21	bdl	bdl	bdl	bdl	bdl	bdl	8.73 ± 2.73	5.84 ± 1.12
BaO	na	na	na	na	na	bdl	0.22	bdl	na	na	na	0.14 ± 0.10	0.27 ± 0.17
Na_2O	bdl	bdl	bdl	0.05	bdl	bdl	0.10	bdl	bdl	bdl	bdl	0.15 ± 0.12	0.32 ± 0.18
K_2O	bdl	bdl	bdl	bdl	bdl	bdl	20.1	bdl	bdl	bdl	0.05	3.91 ± 1.19	6.53 ± 2.05
P_2O_5	bdl	0.25	bdl	bdl	bdl	bdl	0.09	0.09	na	na	na	4.42 ± 1.30	5.86 ± 2.32
Cr_2O_3	bdl	bdl	bdl	bdl	bdl	bdl	bdl	bdl	0.1	0.05	bdl	bdl	bdl
V_2O_3	bdl	bdl	bdl	bdl	bdl	na	na	bdl	0.12	0.12	bdl	na	na
SO_3	bdl	bdl	bdl	bdl	bdl	bdl	bdl	na	na	na	na	bdl	0.12 ± 0.06
Total	99.36	99.69	100.14	98.28	99.69	98.6	101.07	99.93	99.44	99.56	101.80		
Atomic proportion per formula unit (a.p.f.u.)													
Si	1.00	0.98	1.01	1.00	1.00	1.00	2.02	0.87	0.01	0.03	0.02		
Ti	–	–	–	–	–	–	–	0.02	0.02	0.03	0.01		
Al	0.01	0.01	0.01	0.01	0.01	–	0.98	0.31	1.69	0.44	0.02		
Fe^{3+}	–	–	–	–	–	–	–	1.86	0.30	1.49	1.94		
Fe^{2+}	1.78	1.88	1.66	1.64	1.90	–	0.03	4.78	0.90	0.95	0.98		
Mn	0.13	0.07	0.17	0.20	0.02	–	–	0.11	0.03	0.03	0.02		
Mg	0.07	0.04	0.13	0.80	0.06	–	–	0.06	–	0.01	–		
Ca	0.01	0.01	0.02	0.60	0.01	–	–	–	–	–	–		
Ba	–	–	–	–	–	–	–	–	–	–	–		
Na	–	–	–	–	–	–	0.01	–	–	–	–		
K	–	–	–	–	–	–	0.92	–	–	–	–		
P	–	0.01	–	–	–	–	–	0.01	–	–	–	–	
Cr	–	–	–	–	–	–	–	–	–	–	–		
V	–	–	–	–	–	–	–	–	–	–	–		
S	–	–	–	–	–	–	–	–	–	–	–		
O^{2-}	4.00	4.00	4.00	4.00	4.00	2.00	6.00	10.00	4.00	4.00	4.00		

* - In the glass analyses, all iron was calculated to Fe_2O_3 as the ratio of FeO/Fe_2O_3 was not measured

ol: olivine; gls: glass; spl: spinel; isc: iscorite; lct: leucite; qz: quartz; bdl: below detection limit; na: not analyzed

Glass The glass was observed in all analyzed samples. In most cases, the glass chemistry analysis was impossible due to its small size or nuclei of crystallization within the glassy phase. EPM analyses were possible only in KG1 and BZI slags. The glass in these slags consists mainly of SiO_2 (av. 40.70 and 44.93 wt.%), Fe_2O_3 (av. 18.94 and 20.05 wt.%), and Al_2O_3 (av. 20.65 and 15.81 wt.%) in BZI and KG1 respectively Table 2). Concentrations of CaO (av. 5.84 and 8.73 wt.%), P_2O_5 (av. 5.86 and 4.42 wt.%), and K_2O (av. 6.53 and 3.91 wt.%), MnO (av. 0.97 and 1.40 wt.%) was also observed in BZI and KG1 slags respectively (Table 2).

Age

Based on the $^{12}C/^{14}C$ isotope ratio, the age of the charcoal taken from the STAR1 sample was calculated to be 2090 ± 30 BP. As a result of the calibration of the result using the IntCal20 calibration curve, the calendar age was estimated to be in the range of 196 BC–4AD (95.4% probability). With a 91.4% probability, the age of charcoal is 178–38 BC, with a median age of 102 BC with a (1-sigma) uncertainty of ± 50 BC (Additional file 2).

Smelting conditions

Temperature

Two phase diagrams that best fitted the chemistry of the samples (Table 2) were used for the slags' liquidus temperature estimations: CaO–SiO_2–FeO-6 wt.%Al_2O_3 (92.10–97.53 wt.% of elements included) and FeO–SiO_2–Al_2O_3 (89.63–97.03 wt.% of elements included). CaO–SiO_2–FeO-6 wt.%Al_2O_3 and FeO–SiO_2–Al_2O_3 show similar results with liquidus temperatures in the ranges of 1160 to 1250 °C and 1150–1200 °C respectively (Table 3; Fig. 5).

Discussion

Age

The radiocarbon dating uses $^{14}C/^{12}C$ ratios in the analyzed carbonaceous material. In the case of iron metallurgy, isotope ratios may be disturbed due to the addition of C from another source in the production process. By using siderite ores ($FeCO_3$) or fluxes in the form of calcite ($CaCO_3$), carbon with an isotopic age exceeding 10,000 years could be introduced into the metallurgical

Table 3 Summary of the conditions prevailing during the formation of the analyzed slags

	STAR1	KG1	KG2	BZI	JI
CaO–SiO_2–FeO–6 wt.%Al_2O_3 diagram [°C] [33]	1200–1250	~ 1160	1200–1250	~ 1160	1160–1180
FeO–SiO_2–Al_2O_3 diagram [°C] [35]	1150–1200	1150–1200	1150–1200	1150–1200	1150–1200
Viscosity [Pa s]	0.22–0.15 at 1150–1200 °C	1.02–0.67 at 1150–1200 °C	0.26–0.18 at 1150–1200 °C	0.71–0.32 at 1150–1200 °C	0.41–0.28 at 1150–1200 °C
RII	0.57	1.13	0.62	0.96	0.77
Oxygen fugacity (logP O_2) [atm.]	− 13.20 to − 12.53				

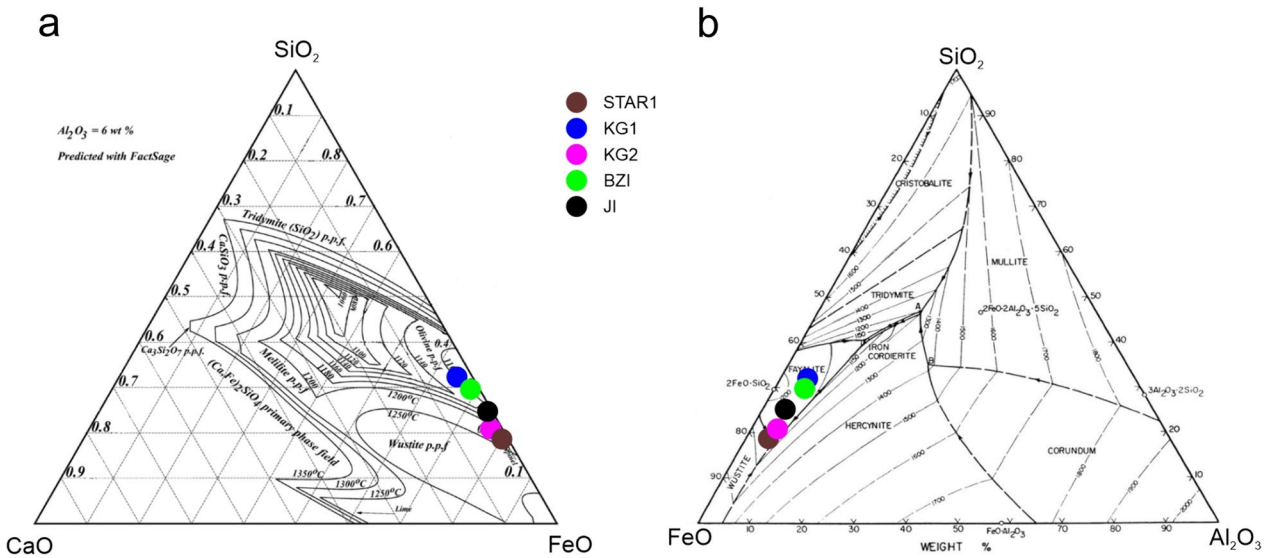

Fig. 5 Phase diagrams with the marked slags' chemical composition (**a**—[33, 34]; **b**—[35])

charge [36, 37]. However, the analyzed slags contain only up to 2.47% CaO, proving that no calcite was added as a flux. Moreover, during smelting, carbonates in the charge decompose at temperatures well below the liquidus temperature of the analyzed slags [38, 39]. Isotope analyses of charcoal are also subject to errors related to the old wood effect [36]. However, considering the large scope and extended period of operation of the Holy Cross Mountains center [21], the metallurgists of that time had to conduct appropriate forest management. In such large centers, trees up to several dozen years old were used for charcoal production, limiting the negative impact on the age determined by ^{14}C analyses [36].

The analysis of charcoal found in the slag gave the date of 196 BC–4 AD, falling within the range of isotope analyses conducted so far, i.e., 300 BC-200 AD [21]. This confirms that the analyzed slags were formed during the Roman influence period, which was characterized by increased metallurgical activity in the areas of present-day Poland [21, 40–42]. Apart from the Holy Cross Mountains, there were many smaller metallurgical centers in Poland. Isotope analyses show that iron smelting in Masovia was carried out in the period covering at least 2450–1890 BP [41], with the greatest development occurring in the first two centuries AD [40]. In Lower Silesia (Poland), the first traces of metallurgical activity date back to the third-first century BC [42]. Dating of iron objects from Nowe Brzesko (Lesser Poland Voivodeship) gave an age in the range of 217–412 AD [37].

Homogeneity of the metallurgical process

Temperature

Temperature is the most critical parameter to be determined when reconstructing historical metallurgical processes. Temperature conditions affect the oxidation–reduction conditions and the melt's viscosity [2, 44]. These three parameters, combined with ore properties, determine the smelting efficiency. The most commonly used method of determining the smelting temperature is estimating the slags' liquidus temperature [45–47]. Considering that the slags were formed from the melt, the minimum temperature at which the process was carried out could not be lower than the liquidus temperature [45]. The liquidus temperature of the analyzed slags was determined based on phase diagrams (Table 3; Fig. 5). All of the analyzed slags consist mainly of FeO and SiO_2, with a small addition of Al_2O_3. Together, these elements account for 90–97 wt.% of the sample (Table 1). In such circumstances, the phase diagram FeO-SiO_2-Al_2O_3 should provide the best temperature estimations with little error due to its excellent fit to the data.

Based on the analyses performed, it can be concluded that in all cases, the temperature during smelting, regardless of location, was similar (1150–1200 °C; Table 3). A similar temperature in the 1130–1260 °C range was determined for most (19 out of 23) of the samples from the Holy Cross Mountains analyzed by Holewinski in the 1950s [21]. The remaining samples are characterized by higher temperatures (1370–1430 °C) due to larger SiO_2 content [21], which could be caused by the contamination of samples with furnace/pit walls material, similar to sample STAR2 described in this study (Table 1; Fig. 3).

Iron production occurred in several metallurgical centers in present-day Poland during a similar period. These include, in addition to the area of the Holy Cross Mountains, centers located in Mazovia (Milanówek/Falęcin) [18], Tarchlice (Lower Silesia) [18, 43], and Opole [18], among others. The liquidus temperature of Mazovia and Tarchlice slags is similar to that of analyzed slags (1150–1200 °C; Table 4). In slags from Opole, the temperature determined for the averaged chemical composition [18] is significantly higher (1050–1400 °C; Table 4) due to the larger content of Al_2O_3 (4.20–18.70 wt.%), and SiO_2 (11.50–34.65 wt.%), which increase the liquidus temperature [35]. Again, possible contamination of slag with furnace material should be considered.

Table 4 Comparison of the properties of slags after bloomery iron production

	Age	Liquidus temperature [°C]	Viscosity [Pa s]**	logP O_2***	RII
This Study	196 BC–4 AD	1150–1200	0.15–1.02	– 13.20 to – 12.53	0.57 to 1.13
Holy Cross Mountains [21]	300BC–400AD	1130–1430	0.08–0.76	– 13.48 to – 10.03	0.67–2.05
Tarchlice[18]	Roman period	1150–1200*	0.48–1.77	– 13.20 to – 12.53	0.98–1.39
Opole [18]	2–5 century AD	1050–1400*	0.13–2.08	– 14.71 to – 10.31	av. 1.01
Mazovia (Milanówek/Falęcin) [18, 43]	Ancient period	1150–1200*	0.07–1.24	– 13.20 to – 12.53	0.72–0.81

* Determined using FeO-SiO_2-Al_2O_3 diagram

** Calculated using BBHLW model,

*** Calculated for liquidus temperatures using SLAG software

Oxidizing-reducing conditions

The oxidation–reduction conditions prevailing during smelting can be determined based on the phase composition of the slags. By observing which phases have been reduced/oxidized, we can determine the minimum and maximum conditions of oxygen fugacity [2, 44, 47, 48]. In the case of slags after bloomery iron production, we cannot rely on the presence of oxidized/metallic phases of various metals because, apart from Fe, other metals that could be reduced do not occur in sufficient quantities in these slags (Table 1; Additional file 3). Regarding phase composition, slags after iron production are similar and consist mainly of olivine with lower amounts of other phases [48–50]. Taking into account the fact that in each case, oxidized Fe (mainly as FeO) in the form of oxides or silicates is observed in the slags, as well as the fact that metallic iron was formed during smelting, the maximum value of oxygen fugacity depends on the state of equilibrium between Fe and FeO. The fugacity of oxygen (logP O_2) at which thermodynamic equilibrium occurs between metallic iron and FeO for temperatures 1150–1200 °C is from − 13.20 to − 12.53 [32]. These are the maximum values at which the reduction of iron oxides to the metallic phase is possible [32]. Since both the Fe-bearing phases (Fig. 3) and liquidus temperature (Table 3) do not differ between analyzed samples, there are no differences in the calculated oxygen fugacity between samples as well (Table 3). Due to the similar liquidus temperature, the maximum oxygen fugacity at which FeO can be reduced to metallic iron is also similar to the values for most of the slags from the Holy Cross Mountains area, Mazovia and Tarchlice (Table 4). In case of Ople location higher range of liquidus temperature of the slags results in the broader oxygen fugacity range: − 14.71 to − 10.31 (Table 4).

The reduction process is also time-dependent. Limited melting time negatively affects reduction efficiency. This dependence forces the creation of a more reducible environment during smelting than required by the thermodynamic equilibrium between the metallic and oxide phases. For this reason, the amount of metal produced depends on how far oxidation–reduction conditions deviate from the equilibrium state and move toward a more reducing environment. The more reducing environment, the amount of Fe remaining in the slag (in oxidized form) is lower. The model proposed by Charlton et al. [51] was used to estimate how strongly reducing the environment prevailed during the studied smelting process:

$$RII = \frac{2.39 * SiO_2}{FeO + MnO}$$

The Reducible Iron Index (RII) is correlated with the oxidation–reduction conditions. The higher the value, the more reductive the environment was during smelting [51]. In all cases, the RII value was 0.57–1.13 in the analyzed slags.

The most reductive conditions occurred during the formation of slag KG1 (1.13) and the least in the case of slag STAR1 (0.57) (Table 3). Comparing the results obtained for other slags from the Holy Cross Mountains [21] shows that the RII index (0.67–1.32) in most cases is similar to the data presented in this study (Table 4). Only two samples are characterized by higher values (ca. 2.0) ([21]; Table 4). The RII value given for the average chemical composition of slags from Opole and Mazovia is within the range marked for slags from the area of the Holy Cross Mountains (0.72–1.01; Table 4). The RII values of slags from Tarchlice (0.98–1.39) seem to be slightly higher; however, they are still within the range of the previously studied slags from the area of the Holy Cross Mountains (Table 4). Similar RII values suggest that similarly reducing conditions prevailed in all locations. However, it should be remembered that the RII value also depends on the metallurgical charge's chemical composition and the melt's possible contamination [51].

Viscosity

Viscosity affects the ability of metallic phases to separate from smelting by-products (e.g. slags) [2, 44, 47]. The presented study determined the melt viscosity using the BBHLW model (named after Browning, Bryant, Hurst, Lucas, and Wall) [52]. This model was designed based on coal ash, smelting, and synthetic slags covering materials with a broad chemical composition (including 18.5–70.0 wt.% of SiO_2, 0–80.0 wt.% of FeO) [53]. Since a high FeO content characterized the analyzed slags, the BBHLW model seems the most appropriate. Viscosity in the range of liquidus temperatures of slags was 0.15–1.02 Pa s (at 1150–1200 °C; Table 3; Fig. 6).

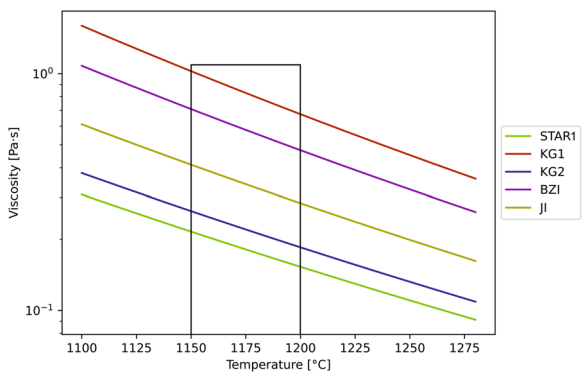

Fig. 6 Viscosity graph obtained from BBHLW model for analyzed slags with liquidus temperature ranges marked

The viscosity of the analyzed slags is similar to the viscosity calculated for the slags from other Holy Cross Mountains locations (0.08–0.76 Pa s) and Mazovia (0.07–1.24 Pa s) (Table 4). Slags from Tarchlice have slightly higher viscosity (0.48–1.77 Pa s; Table 4). Slags from Opole are characterized by a wider viscosity range than others. This is due to the broader temperature range in which the calculations were made (1050–1400 °C). At the lowest temperatures, the viscosity was significantly higher than in the other locations (2.08 Pa s). In addition, a relatively large amount of Al_2O_3 in these slags also affects the viscosity results [18].

Cooling rate

The morphology of olivine crystal can be used to determine the cooling rate of the silicate melt, which is the slag precursor [44, 54]. In the KG1-2, STAR1-2, and JI slags, tabular olivine crystals (Fig. 4d) corresponding to granular olivine described by Donaldson [54] were observed. These are formed at a low 5 °C/h temperature gradient [54]. Elongated olivine crystals were observed in the STAR1-2, JI, and BZI slags (Fig. 4f,h), resembling chain and lattice olivine that crystallize at temperature gradients reaching 80 and 300 °C/h, respectively [54]. The difference in olivine morphologies in STAR1-2 and JI slags indicates the variety of temperature gradients during slag melt cooling. No fiber olivine was distinguished, indicating that the cooling rate never reached 1450 °C/h [54]. Similar variation in olivine crystal habit was described at other locations where bloomery iron production was carried out [55–57].

During the production of iron in the Holy Cross Mountains, the slag flowed down to the bottom of the furnace, from where it was not removed [21]. This procedure allowed for slow cooling of the slag melt, especially considering the volume and mass of the singular slag portions found in the Holy Cross Mountains, reaching up to 120 kg [25]. Still, the slag melt on contact with the pit walls was subjected to faster cooling, hence the varied morphology of olivine crystals (Fig. 4).

Conclusions

The obtained data proves that the conditions under which the smelting process was carried out in varied locations across the Holy Cross Mountains were uniform. Slags were formed at 1150–1200 °C with logP O_2 from − 13.20 to − 12.53. Melt viscosity is comparable in all samples (0.15–1.02 Pa s). The lack of differences between the slags was also noticeable in the cooling rate. The slag crystallized at a rate of 5 to 300 °C/h. The ancient (196 BC—4AD) origin of the slags was confirmed based on the $^{12}C/^{14}C$ isotope ratios of the charcoal found in the STAR1 slag.

Similarities between metallurgy in the Holy Cross Mountains and other ancient bloomery iron production centers in Poland are evident. Liquidus temperature, oxygen fugacity, and viscosity are consistent with data calculated for other Holy Cross Mountains, Mazovia, and Tarchalice locations. One of the ancient metallurgical locations considered in the publication (Opole) could be using slightly different conditions during smelting. Still, considering the high Al_2O_3 content in the slags from Opole, it is likely that the differences in liquidus temperature, oxygen fugacity, and viscosity result from contamination of the slag with the material building the walls of the furnace/pit.

Supplementary Information

The online version contains supplementary material available at https://doi.org/10.1186/s40494-024-01266-6.

Additional file 1. Detection limits and EPMA measurement conditions.

Additional file 2. Details (standards used) regarding slag chemical composition measurements and EPMA analyses and the result of radioisotope dating.

Additional file 3. Chemical composition of slags including trace elements and quality assurance/quality control (QA/QC).

Acknowledgements

This study was supported by the National Science Center (NCN) Grant No. 2019/35/O/ST10/00313. We would like to thank the Museum of Nature and Technology in Starachowice for providing material for the study.

Data citation

No dataset from external repositories was used in this study. All existing data used for this publication are cited in the reference section.

Author contributions

Conceptualization: K.K., R.W., and A.G.; methodology: K.K., R.W., A.G.; Writing—original draft preparation: K.K.; writing—review and editing: K.K., R.W., and A.G.; resources: K.K., R.W., and J.J.; figures, tables, and additional files: K.K. and R.W. All authors read and approved the manuscript.

Funding

This research was funded by the National Science Center (NCN) Grant No. 2019/35/O/ST10/00313.

Data availability

The data that supports the finding of the study is given in the tables and figures within the main text and in additional files. This study brought together existing data from several different sources, which are cited throughout.

Declarations

Competing interests

The authors declare no competing interests.

Received: 5 January 2024 Accepted: 29 April 2024
Published online: 08 May 2024

References

1. Mikoda B, Kucha H, Potysz A, Kmiecik E. Metallurgical slags from Cu production and Pb recovery in Poland—their environmental stability and

resource potential. Appl Geochem. 2018;98:459–72. https://doi.org/10.1016/j.apgeochem.2018.09.009.
2. Kupczak K, Warchulski R, Gawęda A. Reconstruction of smelting conditions during 16th-to 18th-century copper ore processing in the Kielce region (Old Polish Industrial District) based on slags from Miedziana Góra, Poland. Archaeometry. 2023;65:547–69. https://doi.org/10.1111/arcm.12837.
3. Bebermeier W, Brumlich M, Cordani V, de Vincenzo S, Eilbracht H, Klinger J, et al. The coming of iron in a comparative perspective. J Anc Stud. 2016;6:152–89.
4. Hendrickson M, Leroy S, Hua Q, Kaseka P, Vuthy V. Smelting in the shadow of the iron mountain: preliminary field investigation of the industrial landscape around Phnom Dek, Cambodia (ninth to twentieth centuries AD). Asian Perspect. 2017;56:55–91.
5. Hendrickson M, Leroy S, Castillo C, Hua Q, Vega E, Phon K. Forging empire: angkorian iron smelting, community and ritual practice at Tonle Bak. Antiquity. 2019;93:1586–606.
6. Plaza MT, Garrido F, Larreina-García D. A new piece of the puzzle: slag and ore analysis to reconstruct the prehispanic smelting technology at the Atacama Desert, Chile. Herit Sci. 2023;11:171. https://doi.org/10.1186/s40494-023-01017-z.
7. Westner KJ, Klein S, Sergeev D, Müller M. Temperature estimates of historical Pb–Ag smelting slags: a multi-methodological approach. J Archaeol Sci Rep. 2022;46:103654. https://doi.org/10.1016/j.jasrep.2022.103654.
8. Stepanov I, Borodianskiy K, Eliyahu-Behar A. Assessing the quality of iron ores for bloomery smelting: laboratory experiments. Minerals. 2019;10:33.
9. Whiteman J, Okafor EE. Characterization of Nigerian bloomery iron smelting slags. Hist Metall. 2003;37:71–84.
10. Metz O, Bohr R. Theoretical and practical aspects of iron smelting in a bloomery furnace. Mining archaeology: perspectives, conflicts, challenges. In: Proceedings of the 10th International Symposium on Archaeological Mining History Yearbook of the Institute Europa Subterranea Institute Europa Subterranea. 2015. p. 8–21.
11. Li S, Li Y, Zhu R, Wang H. Analysis on ancient bloomery ironmaking technology: the earliest ironmaking evidence in the central plains of China was taken as the research object. Metals. 2022;12:1307.
12. Zou G, Min R, Cui J, Ma R, Zhou X, Yang C. The special iron making in Southwest China around the 10th CE: Scientific evidence from an iron smelting site in Erhai lake area, Yunnan province. J Cult Herit. 2019;37:266–72.
13. Stepanov IS, Sauder L, Keen J, Workman V, Eliyahu-Behar A. By the hand of the smelter: tracing the impact of decision-making in bloomery iron smelting. Archaeol Anthropol Sci. 2022;14:80.
14. Pernet-Fisher JF, Day JMD, Howarth GH, Ryabov VV, Taylor LA. Atmospheric outgassing and native-iron formation during carbonaceous sediment–basalt melt interactions. Earth Planet Sci Lett. 2017;460:201–12. https://doi.org/10.1016/j.epsl.2016.12.022.
15. Goldstein JI, Scott ERD, Chabot NL. Iron meteorites: crystallization, thermal history, parent bodies, and origin. Geochemistry. 2009;69:293–325. https://doi.org/10.1016/j.chemer.2009.01.002.
16. Peacock CL, Lalonde SV, Konhauser KO. Iron minerals as archives of Earth's redox and biogeochemical evolution. In: Ahmed IAM, Hudson-Edwards KA, editors. Redox-reactive minerals: properties, reactions and applications in clean technologies, vol. 17. Strasbourg: European Mineralogical Union; 2017. p. 113–63.
17. Johnson D, Tyldesley J, Lowe T, Withers PJ, Grady MM. Analysis of a prehistoric Egyptian iron bead with implications for the use and perception of meteorite iron in ancient Egypt. Meteorit Planet Sci. 2013;48:997–1006. https://doi.org/10.1111/maps.12120.
18. Thelemann M, Bebermeier W, Hoelzmann P, Lehnhardt E. Bog iron ore as a resource for prehistoric iron production in Central Europe—a case study of the Widawa catchment area in eastern Silesia, Poland. Catena. 2017;149:474–90. https://doi.org/10.1016/j.catena.2016.04.002.
19. Orzechowski S. Socioeconomic determinants of iron production on Polish lands during antiquity: the phenomenon of metallurgical smelting centres of the Przeworsk culture. Archeologické Rozhledy. 2018;70:391–403.
20. Samsonowicz A, Wyczański A, Tazbir J, Staszewski J, Kizwalter T, Nałęcz T, Paczkowski A, Chwalba A. History of Poland. Poland until 1586. Warszawa: Wydawnictwo Naukowe PWN; 2007. p. 623.
21. Bielenin K. Ancient mining and iron smelting in the Holy Cross Mountains. 2nd ed. Kielce: Kieleckie Towarzystwo Naukowe, Towarzystwo Przyjaciół Górnictwa, Hutnictwa i Przemysłu Staropolskiego w Kielcach; 1992. p. 1–267.
22. Janiec J, Kardyś P. Raw material base of ancient metallurgy in the in the Holy Cross Mountains region—an attempt at a different perspective. Świętokrzyskie—Environment, Cultural Heritage, Regional Education. WBP Kielce. 2021;27:173–82.
23. Orzechowski S. Experimental research on the reconstruction of the smoke-making process in the Holy Cross Mountains—scientific and educational significance of the experiment. Skanseny Archeologiczne I Archeologia Eksperymentalna. 2012. p. 307–29.
24. Wrona A. The production of high carbon steel directly in bloomery process: theoretical bases and metallographic analyses of the experiments results. EXARC J. 2013;2:1–16.
25. Orzechowski S. Settlement base and raw material bases of ancient metallurgy in the in the Holy Cross Mountains region. Kieleckie Towarzystwo Naukowe; 2007. p. 1–391
26. Geoportal. https://www.geoportal.gov.pl. Accessed 20 Dec 2023.
27. Heliasz Z, Ostaficzuk S. Historical residues of iron ore mining in environs of the Holy Cross Mountains (the Góry Świętokrzyskie) are recognizable on the Digital Terrain Elevation Model (DEM) derived from the LIDAR data. Gospodarka Surowcami Mineralnymi. 2020;36:161–86. https://doi.org/10.24425/gsm.2020.133946.
28. Samsonowicz J. About the hematite deposit in Rudki near Nowa Słupia. In: Meeting of the Polish Geological Society on November 21; 1922;4:9–10.
29. Fawcett TG, Faber J, Kabbekodu S, McClune F, Rafaja D. 4+, the material identification database. Microstruct Anal Mater Sci. 2005;1–3.
30. Ramsey CB. Bayesian analysis of radiocarbon dates. Radiocarbon. 2009;51:337–60. https://doi.org/10.1017/S0033822200033865.
31. Reimer PJ, Austin WE, Bard E, Bayliss A, Blackwell PG, Ramsey CB, et al. The IntCal20 Northern Hemisphere radiocarbon age calibration curve (0–55 cal kBP). Radiocarbon. 2020;62:725–57. https://doi.org/10.1017/RDC.2020.41.
32. Kupczak K, Warchulski R. SLAG—software for reconstruction of historical smelting processes based on slag properties. Archaeometry. 2024. https://doi.org/10.1111/arcm.12940.
33. Jak E, Hayes P, Pelton A, Decterov S. Thermodynamic modelling of the $A1_2O_3$–CaO–FeO–Fe_2O_3–PbO–SiO_2–ZnO system with addition of K and Na with metallurgical applications. In Proc VIII Int'l Conf on Molten Slags, Fluxes and Salts; Santiago, Chile. 2009. p. 473–90.
34. Gheribi AE, Audet C, Le Digabel S, Bélisle E, Bale CW, Pelton AD. Calculating optimal conditions for alloy and process design using thermodynamic and property databases, the FactSage software and the Mesh Adaptive Direct Search algorithm. Calphad. 2012;36:135–43.
35. Li Y, Zhang M, Li S, Yang F. Evidence of early iron smelting on the Tibetan plateau. Archaeol Anthropol Sci. 2022;14:52. https://doi.org/10.1007/s12520-022-01528-z.
36. Craddock PT, Wayman ML, Jull AJT. The radiocarbon dating and authentication of iron artifacts. Radiocarbon. 2002;44:717–32. https://doi.org/10.1017/S0033822200032173.
37. Hüls CM, Bulas J, Kasiński M, Okońska-Bulas M. First results of metallographic analysis and absolute dating of iron finds from Nowe Brzesko, site 26, Proszowice District. Archaeometry. 2023;65:587–602. https://doi.org/10.1111/arcm.12858.
38. El-Bellihi AA. Kinetics of thermal decomposition of iron carbonate. Egypt J Chem. 2010;53:871–84. https://doi.org/10.21608/EJCHEM.2010.1268.
39. Karunadasa KS, Manoratne CH, Pitawala H, Rajapakse RMG. Thermal decomposition of calcium carbonate (calcite polymorph) as examined by in-situ high-temperature X-ray powder diffraction. J Phys Chem Solids. 2019;134:21–8. https://doi.org/10.1016/j.jpcs.2019.05.023.
40. Woyda S. The Błońska Plain at the end of ancient times. Metallurgical center. Problems of the past of Mazovia and Podlasie. 2004. p. 129–66.
41. Janiszewski R. Before or after? Stratigraphic relations of Iron Age slag-pit furnaces in the Mazovian Centre of Metallurgy. Archeologické Rozhledy. 2018;70:381–90.
42. Wrona P, Różański Z, Pach G, Niewiadomski AP, Veiga JP. Historical outline of iron mining and production in the area of present-day Poland. Minerals. 2021;11:1136. https://doi.org/10.3390/min11101136.

43. Woźniak M. Milanówek/Falęcin–a settlement of iron-smelters from the Late Antiquity. Archeologické Rozhledy. 2018;70:363–80.
44. Warchulski R, Szczuka M, Kupczak K. Reconstruction of 16th—17th century lead smelting processes on the basis of slag properties: a case study from Sławków, Poland. Minerals. 2020;10:1039. https://doi.org/10.3390/min10111039.
45. Kądziołka K, Pietranik A, Kierczak J, Potysz A, Stolarczyk T. Towards better reconstruction of smelting temperatures: methodological review and the case of historical K-rich Cu-slags from the Old Copper Basin, Poland. J Archaeol Sci. 2020;118:105142. https://doi.org/10.1016/j.jas.2020.105142.
46. Derkowska K, Świerk M, Nowak K. Reconstruction of copper smelting technology based on 18–20th-century slag remains from the Old Copper Basin, Poland. Minerals. 2021;11:926. https://doi.org/10.3390/min11090926.
47. Warchulski R, Kupczak K, Gawęda A, Sitko R. Complete reconstruction of the process and conditions during gold smelting in the 15–17th century in Złoty Stok based on metallurgical slags. Archaeometry. 2022;64:916–634. https://doi.org/10.1111/arcm.12752.
48. Crabb S. How did the iron industry in Southern Britain change from the Iron Age to the Roman period? [PhD Thesis]. University of Oxford; 2018. p. 1–376.
49. Kramar S, Lux J, Pristacz H, Mirtič B, Rogan-Šmuc N. Mineralogical and geochemical characterization of Roman slag from the archaeological site near Mosnje (Slovenia). Mater Technol. 2015;49:343–8. https://doi.org/10.17222/mit.2013.299.
50. Nakanishi A. Mössbauer study of ancient iron smelting slag in Japan. Hyperfine Interact. 2008;186:135–9. https://doi.org/10.1007/s10751-008-9843-1.
51. Charlton MF, Crew P, Rehren T, Shennan SJ. Explaining the evolution of ironmaking recipes—an example from northwest Wales. J Anthropol Archaeol. 2010;29:352–67. https://doi.org/10.1016/j.jaa.2010.05.001.
52. Browning GJ, Bryant GW, Hurst HJ, Lucas JA, Wall TF. An empirical method for the prediction of coal ash slag viscosity. Energy Fuels. 2003;17:731–7. https://doi.org/10.1021/ef020165o.
53. Bronsch A. Viscosity of slags [PhD Thesis]. Dissertation, Freiberg, Technische Universität Bergakademie Freiberg, 2017. p. 1–238.
54. Donaldson CH. An experimental investigation of olivine morphology. Contrib Mineral Petrol. 1976;57:187–213. https://doi.org/10.1007/BF00405225.
55. Portillo-Blanco H, Zuluaga MC, Ortega LA, Alonso-Olazabal A, Cepeda-Ocampo JJ, Martínez SA. Mineralogical characterization of slags from the Oiola Site (Biscay, Spain) to assess the development in bloomery iron smelting technology from the Roman Period to the Middle Ages. Minerals. 2020;10:321. https://doi.org/10.3390/min10040321.
56. Larreina-Garcia D, Li Y, Liu Y, Martinon-Torres M. Bloomery iron smelting in the Daye County (Hubei): technological traditions in Qing China. Archaeol Res Asia. 2018;16:148–65. https://doi.org/10.1016/j.ara.2018.10.001.
57. Portillo H, Zuluaga MC, Ortega LA, Alonso-Olazabal A, Murelaga X, Martinez-Salcedo A. XRD, SEM/EDX and micro-Raman spectroscopy for mineralogical and chemical characterization of iron slags from the Roman archaeological site of Forua (Biscay, North Spain). Microchem J. 2018;138:246–54. https://doi.org/10.1016/j.microc.2018.01.020.

Publisher's Note